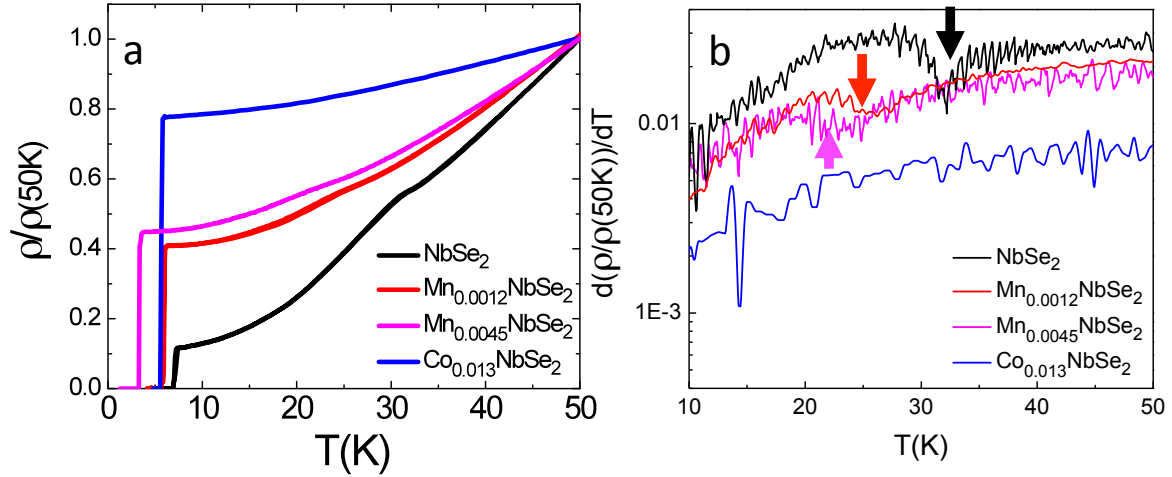
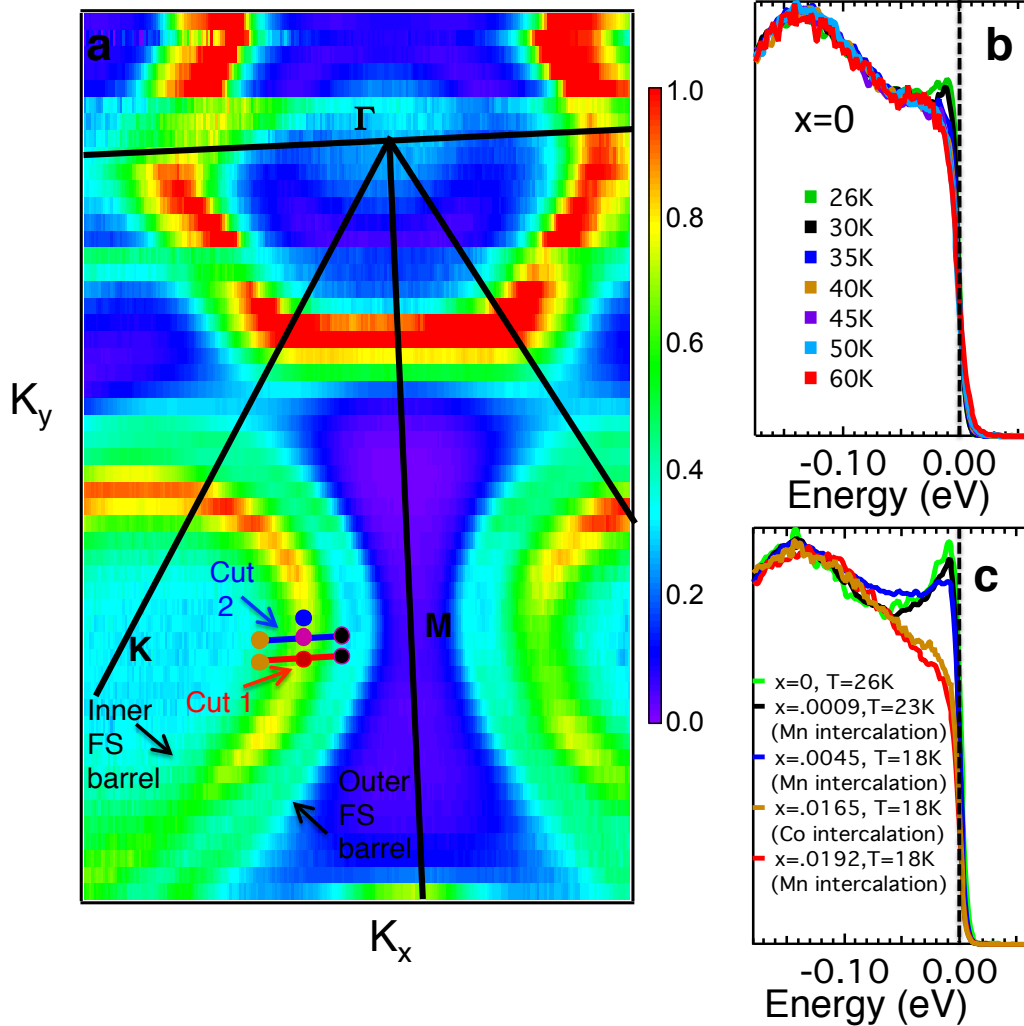


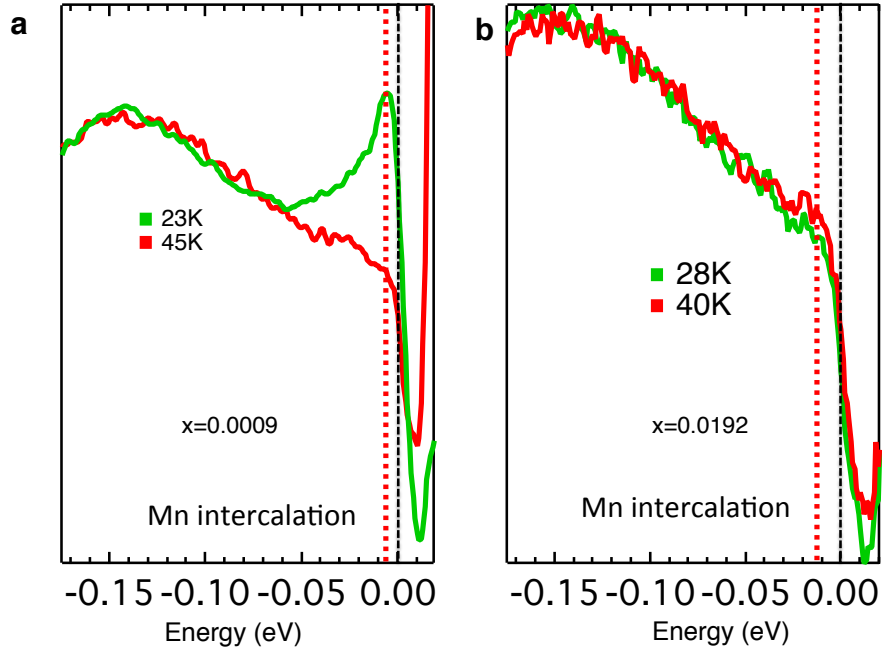
Supplementary Figure 1 | Magnetization versus temperature curves for pristine and intercalated 2H-NbSe₂ samples. Superconducting transition for different values of x .



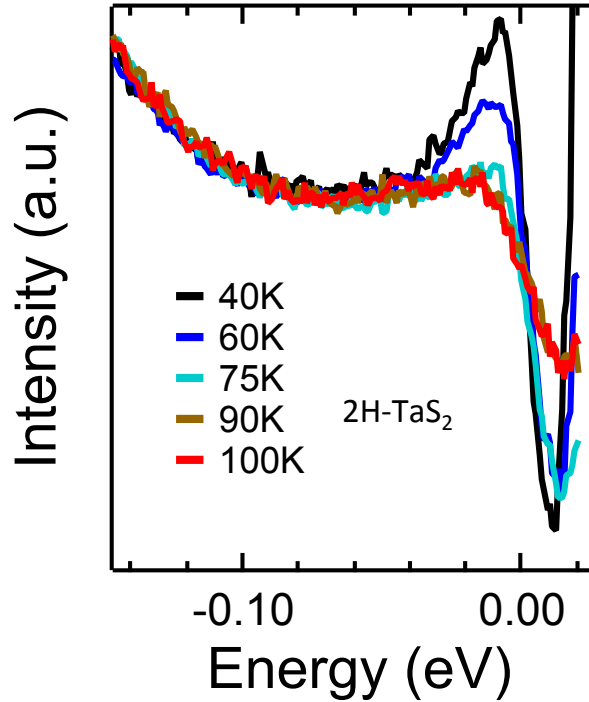
Supplementary Figure 2 | Transport data on pure and intercalated samples. (a) Resistivity normalized to its value at 50K for $x=0$, 0.0012 (Mn intercalated), 0.0045 (Mn intercalated) and 0.013 (Co intercalated). (b) Temperature derivative of the ρ vs T plot of the data presented in (a). Arrows indicate the CDW transition temperature. The sample with $x=0.013$ does not show any appreciable change in the first derivative of the resistivity data.



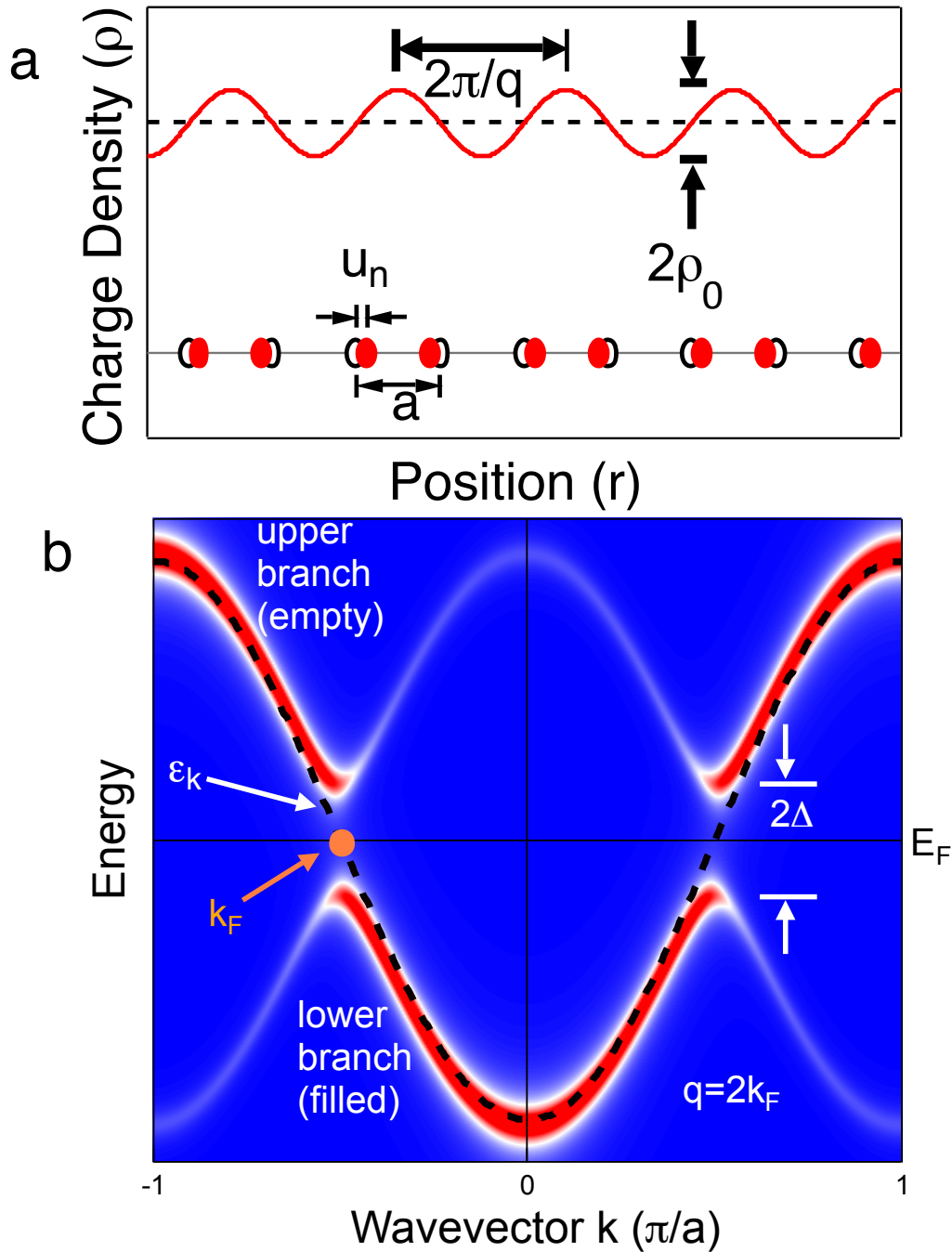
Supplementary Figure 3 | Raw ARPES data: (a) Raw ARPES intensity map at zero binding energy (integrated over an energy window of 10 meV) as a function of k_x and k_y for an $x=0$ sample exhibiting double walled Fermi surfaces centered around the Γ as well as the K point. As shown in Fig. 2d, cut 1 is along the red line, while cut 2 is along the blue line. Data in Figs. 2a, 2b are taken along cut 1 and Fig. 2c along cut 2. Raw EDCs corresponding to the Fermi function divided ones in (b) Fig. 1b and (c) Fig. 1c. Black dotted lines denote the location of the chemical potential.



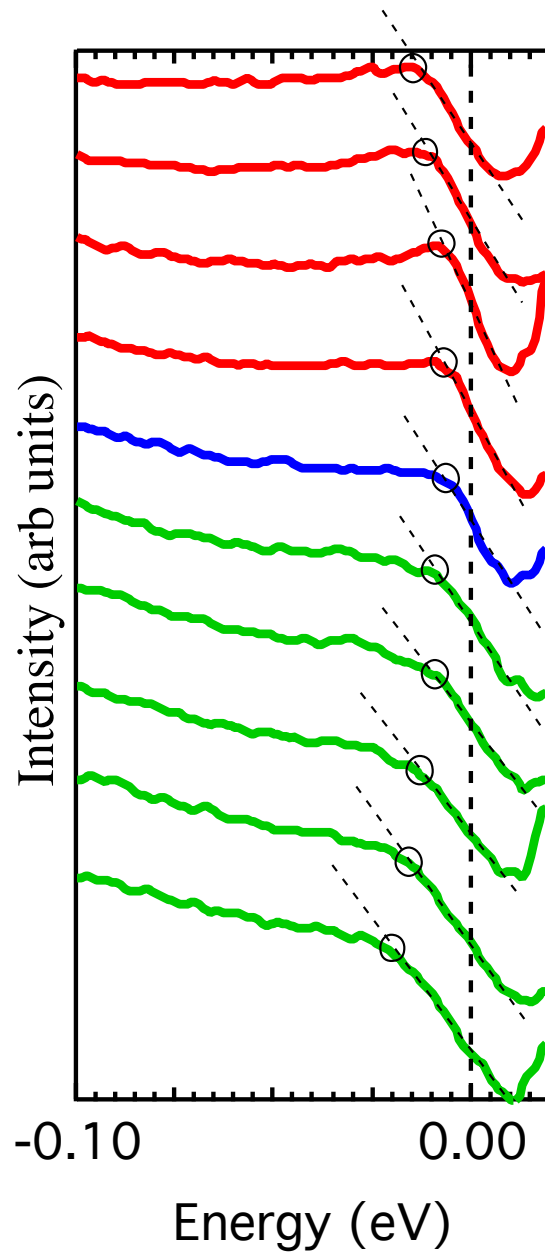
Supplementary Figure 4 | Fermi function divided ARPES data for two different intercalated samples. Temperature dependent Fermi function divided ARPES EDCs for (a) $x=0.0009$ (taken at the red dot in Fig. 2d) and (b) $x=0.0192$ (taken at the blue dot in Fig. 2d). Black dotted lines denote the location of the chemical potential. Red dotted lines are used to indicate the energy gap defined as the location of either the peak or kink (i.e., discontinuous change in slope) in the spectrum.



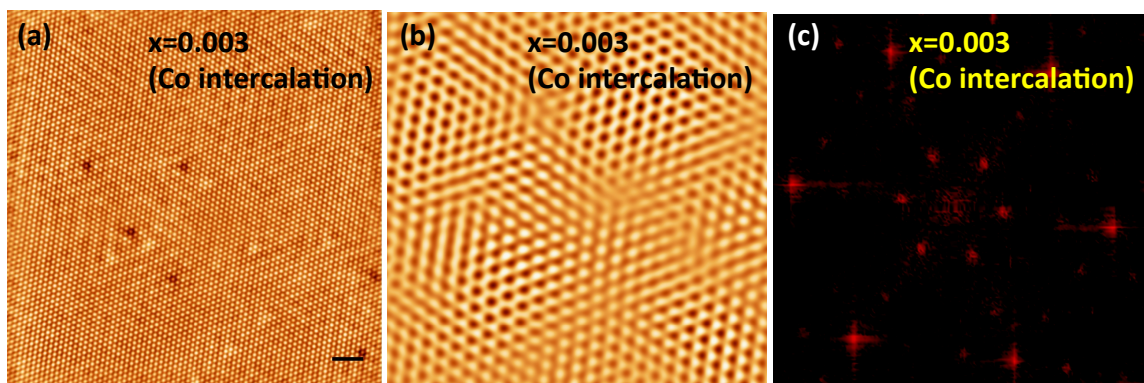
Supplementary Figure 5 | Fermi function divided ARPES data from 2H-TaS₂. Temperature dependent Fermi function divided ARPES EDCs for 2H-TaS₂. ARPES data correspond to the momentum location at which the K-M line intersects the Fermi surface. Like in 2H-NbSe₂ (Fig. 1b of main manuscript), here one can also identify a gap and peak in the spectrum for $T < T_{\text{cdw}}$ ($T_{\text{cdw}} \sim 70\text{K}$) but only a gap for $T > T_{\text{cdw}}$.



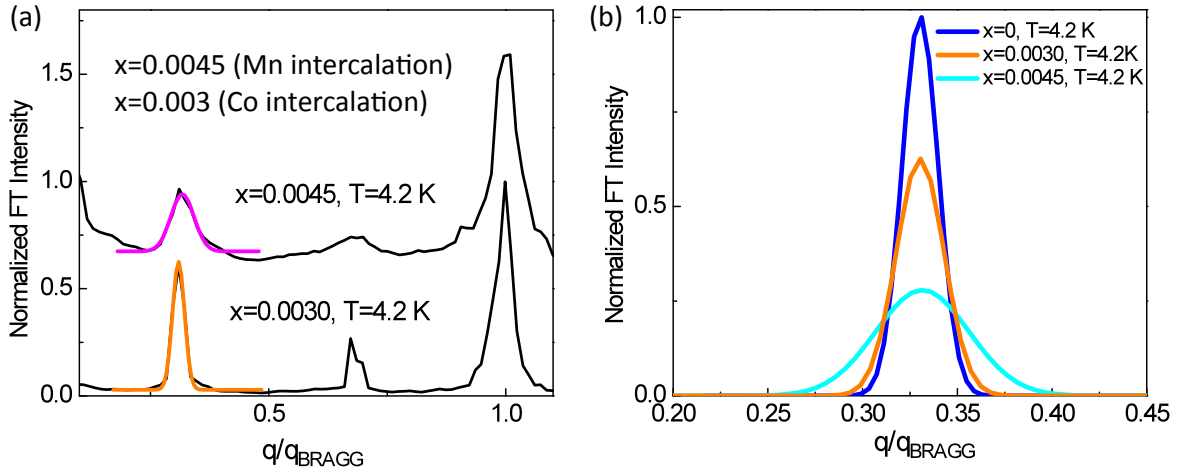
Supplementary Figure 6 | Electronic dispersion in the CDW state associated with a Peierls distortion in a one-dimensional system. (a) A cartoon of one-dimensional CDW order in real space and (b) the corresponding electronic dispersion in momentum space in the normal state (black dotted line) and in the CDW state (red lines).



Supplementary Figure 7 | Identification of peaks and kinks in the ARPES spectra. Demonstration of how dots are selected, particularly when the spectra are not associated with sharp peaks, to investigate bending back of the electronic dispersion in Fig. 2. In particular, we have chosen Fig. 2b in which peak structures of the spectra are not very clear.

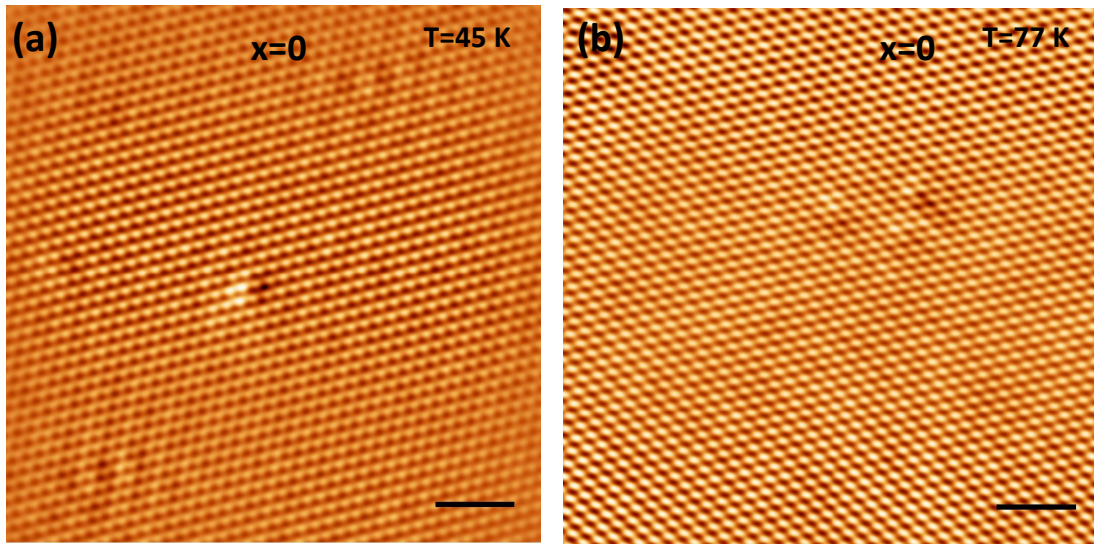


Supplementary Figure 8 | STM of $\text{Co}_{0.003}\text{NbSe}_2$. (a) STM topography image acquired with $V=50$ mV and $I=100$ pA. Scan area is 24 nm x 24 nm (scale bar: 2nm). (b) Fourier filtered image of the topography shown in (a). (c) 2D-FT of the image in (a).



Supplementary Figure 9 | STM Fourier Transform Profiles for different dopants.

(a) Line profiles of the FT of the $\text{Mn}_{0.0045}\text{NbSe}_2$ image (Fig. 3(j) of main text) and the FT of the $\text{Co}_{0.003}\text{NbSe}_2$ image (Supplementary Figure 8c), along one of the lattice wavevector directions. The curves have been shifted for clarity. The intensity of each profile has been normalized to the intensity of the Bragg peak. The CDW peak at $q=q_{\text{BRAGG}}/3$ has been fitted with a Gaussian and the fit is superimposed on the FT line profile for each curve. (b) Gaussian fits of the CDW peaks in $\text{Mn}_{0.0045}\text{NbSe}_2$ and $\text{Co}_{0.003}\text{NbSe}_2$ compared to the CDW peak in pure NbSe_2 .



Supplementary Figure 10 | STM topography of $2H\text{-NbSe}_2$. STM topography images of pure NbSe_2 above the temperature for long range order. Scan areas for both images are $13.5\text{ nm} \times 13.5\text{ nm}$ (scale bars: 2 nm). Tunneling conditions are: $V=50\text{ mV}$ and $I=100\text{ pA}$. (a) $T=45\text{ K}$, (b) $T=77\text{ K}$.

| x | Type of intercalating ion | T_c | T_{cdw} |
|--------|---------------------------|-------|-----------|
| 0 | None | 7.2K | 32.2K |
| 0.0009 | Mn | 6.5K | 29K |
| 0.0012 | Mn | 5.6K | 26.6K |
| 0.0045 | Mn | 3.4K | 23K |
| 0.0192 | Mn | <1.8K | 0K |
| 0.013 | Co | 5.6K | 0K |
| 0.0165 | Co | 4.7K | 0K |
| 0.04 | Co | 3.1K | 0K |

Supplementary Table 1 | Sample details

Concentration of the intercalation ion (x), type of the intercalating ion, superconducting critical temperature (T_c) and T_{cdw} for the samples used in this paper.

Supplementary Note 1

Determination of T_c

We determine the CDW transition temperature T_{cdw} from the CDW induced anomaly in the transport measurements and from the temperature dependence of the CDW order parameter obtained from XRD measurements. We find that these different measurements provide values for T_{cdw} that are close to each other. Supplementary Figure 2 shows resistivity ρ vs temperature T for four samples with $x=0$; $x=0.0012$, $x=0.0045$ (intercalated with Mn); and $x=0.013$ (intercalated with Co), normalized to their individual resistivity at 50K. The derivatives $d\rho/dT$ vs T (Supplementary Figure 2b) for the three samples with $x < x_c$ exhibit clear anomalies, which we identify as the CDW transition temperature T_{cdw} . These transition temperatures agree with the transition temperatures determined as described in the main text from the temperature dependence of the superlattice reflections measured with XRD. The fourth sample with $x > x_c$ does not show any anomaly.

Supplementary Note 2

Raw ARPES data

Supplementary Figure 3a shows the raw ARPES intensity map at zero binding energy (integrated over an energy window of 10 meV) as a function of k_x and k_y . Raw ARPES spectra corresponding to the Fermi function divided ones in Figs. 1b,c are displayed in Supplementary Figures. 3b,c. One can readily observe the energy bands that form two barrels around the K point – the low energy peak/kink corresponds to the inner barrel while the high binding energy “hump” corresponds to the outer barrel (Fig. 2d, Supplementary Figure 3a). For our discussions, we have focused on data in the vicinity of the inner barrel. Supplementary Figure 3b shows a quasiparticle peak that appears at positive binding energy, gets weaker with T , and eventually disappears above T_{cdw} . Similarly, the spectra in Supplementary Figure 3c lose their peak with increasing x , and beyond x_c the peak vanishes. Figure 1b showed the temperature evolution of ARPES spectra across the CDW phase transition. Supplementary Figure 4a shows similar data, i.e. Fermi function divided EDCs taken at the red dot in Figs. 2d, for $x=0.0009$ (Mn intercalation) at temperatures below and above T_{cdw} . The low temperature spectrum has both an energy gap and a peak, while for $T >$

T_{cdw} , the peak disappears but the energy gap remains. Supplementary Figure 4b shows Fermi function divided EDCs at $T=28\text{K}$ and 40K for $x=0.0192$ (Mn intercalation) $> x_c$, taken at \mathbf{k} marked by the blue dot in Fig. 2d. In contrast to Fig. 1b and Supplementary Figure 4a, there is no signature of a peak in Supplementary Figure 4b even at the lowest measured temperatures. Rather there is a kink (marked by the red dotted line) at positive binding energy, with the minimum of the spectrum above the chemical potential, again indicating the presence of an energy gap.

Supplementary Note 3

Loss of coherence at the CDW phase transition in $2H\text{-TaS}_2$

$2H\text{-TaS}_2$, like $2H\text{-NbSe}_2$, exhibits CDW ordering, but with higher transition temperature ($T_{\text{cdw}} \sim 70\text{K}$) (Ref. 1). Our ARPES data measured on $2H\text{-TaS}_2$ (Supplementary Figure 5) shows similar features as that for $2H\text{-NbSe}_2$. The data for $T < T_{\text{cdw}}$ consist of a coherence peak as well as an energy gap, while only an energy gap exists for $T > T_{\text{cdw}}$. Using TEM measurements, it has been shown that CDW fluctuations persist for temperatures much higher than T_{cdw} (Ref. 2). All this suggests that the pseudogap phase induced by phase incoherence is generic to quasi two-dimensional CDW systems.

Supplementary Note 4

Energy gap and backbending of the electronic dispersion in the CDW state

In contrast to superconductors where there is electron-electron pairing, a CDW state is associated with a coupling between electrons and holes, and this is manifested in the electronic dispersion, i.e. the relation between the electronic energy and momentum, below T_{cdw} . As a consequence, the electronic dispersion in the CDW state gets modified from the one in the normal state, i.e. for $T > T_{\text{cdw}}$, and this can be written as^{3,4}:

$$E_{\mathbf{k}} = \frac{1}{2}(\varepsilon_{\mathbf{k}} + \varepsilon_{\mathbf{k}+\mathbf{q}}) \pm \left[\frac{1}{4}(\varepsilon_{\mathbf{k}} - \varepsilon_{\mathbf{k}+\mathbf{q}})^2 + \Delta_{\mathbf{k}}^2 \right]^{1/2}$$

where $\Delta_{\mathbf{k}}$ is the momentum dependent energy gap, $\varepsilon_{\mathbf{k}}$ is the normal state dispersion ($T > T_{\text{cdw}}$) and \mathbf{q} is the CDW wavevector. For simplicity, we consider CDW ordering in a one-dimensional system, noting that there are some important differences between CDW order in 1D and 2D systems, like the fact that the energy gap in the 2D case may be centered away from the Fermi level (as we observe to be the case in $2H\text{-NbSe}_2$). Our primary focus

here is to illustrate the salient experimental signatures associated with the formation of charge order irrespective of dimensionality. The most important of these are the opening of a gap and the related backbending of the electronic dispersion, accompanied by coherence factors, which indicate the amount of mixing between the coupled bands that influence the intensity of the experimental signal. These features are manifested in the 1D case in precisely the same manner as they are in a 2D charge ordered state.

Supplementary Figure 6a shows a schematic of the real space structure of a 1D CDW state, which can be understood as a Peierls instability with a CDW wave vector $\mathbf{q}=2\mathbf{k}_f$, where \mathbf{k}_f is the Fermi momentum. The electronic dispersion of this CDW state, using the equation above, is displayed as the red curves in Supplementary Figure 6b. $E_{\mathbf{k}}$ consists of two branches, which instead of crossing the chemical potential bend downwards/upwards at \mathbf{k}_f . This characteristic bending back of the dispersion provides a direct signature of the electron-hole coupling in the CDW state, with the difference in energy between the lower and the upper branches at \mathbf{k}_f being twice the energy gap, Δ .

Supplementary Note 5

Identification of peaks and kinks in ARPES data

The black dots in Fig.2 correspond to either peaks or the locations of discontinuity, i.e., kinks, in the Fermi function divided ARPES spectra. The procedure for determining the location of the black dots in Figure 2 of the main manuscript is as follows: (i) Whenever there is a discernable peak in the spectrum, it is quite straightforward to select the location of the peak and the black dot corresponds to the peak position. (ii) When there is no well-defined peak we use a simple method: we approximate the leading edge of the spectrum by a straight line and the dot corresponds to that particular energy value at which the straight line starts to deviate from the spectrum. We have considered the data displayed in Fig. 2b, in which the peaks of the spectra are not pronounced, and demonstrated how to determine the locations of black dots in Supplementary Figure 7.

Supplementary Note 6

STM Fourier Transform profiles

In Fig. 3 the 2D-FT of the STM topographic images for samples with different intercalation density are shown. All the images show hexagonal spots corresponding to the Bragg peaks

and the CDW peaks. In Figure 4a, line cuts of the FT along the lattice ordering vector are reported. The intensity of each line cut has been normalized to the intensity of the Bragg peak. In order to quantify the broadening of the CDW peak with the density of intercalating ions (Mn/Co) and the temperature, we fitted the CDW peak with a Gaussian function of the

form: $y = y_0 + \left(\frac{A}{w\sqrt{\pi/2}} \right) \exp(-2x^2/w^2)$, where y_0 is the background of the FT line cut and w

is a width parameter. Figure 4b shows the CDW peak Gaussian fits for the different line cuts. From this figure we observe that the intensity of the CDW peak decreases and the peak broadens with increasing intercalant doping and with increasing temperature. The broadening of this peak measures the loss of translational order.

In the case of pure $2H$ -NbSe₂ above the temperature for long range order, we do observe weak CDW modulations localized around impurities (Supplementary Figure 10a). However, this modulation is very weak and the peaks in the FT are not clearly defined. At $T=77$ K we do not observe any CDW modulations in real space and any CDW peaks in the FT within our resolution, given the low defect density of our samples (Supplementary Figure 10b).

Supplementary Note 7

Effect of different dopants on the CDW order of intercalated $2H$ -NbSe₂

Co and Mn intercalated $2H$ -NbSe₂ crystals with similar doping levels have been characterized with STM. In Supplementary Figure 8 an STM topography image is reported for Co_{0.0030}NbSe₂, together with the FT and the Fourier filtered image. The Fourier filtered image reveals that the CDW lattice forms patches very similar to those obtained in Mn_{0.0045}NbSe₂. The line profile of the FT in Supplementary Figure 8c along a crystal lattice direction is compared with the one obtained for Mn_{0.0045}NbSe₂ (Supplementary Figure 9a), and the fits of the CDW peaks for the two samples are reported in Supplementary Figure 9b. These measurements show that the effect of Co and Mn on the CDW order is the same.

Supplementary References

1. McMillan, W. L., Microscopic model of charge-density waves in $2H\text{-TaSe}_2$.
Phys. Rev. B **16**, 643 –650 (1977).
2. Wagner, K. E., *et al.*, Tuning the charge density wave and superconductivity in Cu_xTaS_2 ,
Phys. Rev. B **78**, 104520 (2008).
3. Gruner, G., *Density waves in solids*. (Perseus Publishing, Cambridge, 1994).
4. Rossnagel, K., On the origin of charge-density waves in select layered transition-metal dichalcogenides. *J. Phys.: Condens. Matter* **23**, 213001 (2011).